Effect of helicity on the correlation time of large scales in turbulent flows

Alexandre Cameron,[*] Alexandros Alexakis,[†] and Marc-Étienne Brachet[‡]
Laboratoire de Physique Statistique, École Normale Supérieure, PSL Research University; Université Paris Diderot Sorbonne Paris-Cité; Sorbonne Universités UPMC Univ Paris 06; CNRS; 24 rue Lhomond, 75005 Paris, France
(Received 15 May 2017; published 6 November 2017)

Solutions of the forced Navier-Stokes equation have been conjectured to thermalize at scales larger than the forcing scale, similar to an absolute equilibrium obtained for the spectrally truncated Euler equation. Using direct numeric simulations of Taylor-Green flows and general-periodic helical flows, we present results on the probability density function, energy spectrum, autocorrelation function, and correlation time that compare the two systems. In the case of highly helical flows, we derive an analytic expression describing the correlation time for the absolute equilibrium of helical flows that is different from the $E^{-1/2}k^{-1}$ scaling law of weakly helical flows. This model predicts a new helicity-based scaling law for the correlation time as $\tau(k) \sim H^{-1/2}k^{-1/2}$. This scaling law is verified in simulations of the truncated Euler equation. In simulations of the Navier-Stokes equations the large-scale modes of forced Taylor-Green symmetric flows (with zero total helicity and large separation of scales) follow the same properties as absolute equilibrium including a $\tau(k) \sim E^{-1/2}k^{-1}$ scaling for the correlation time. General-periodic helical flows also show similarities between the two systems; however, the largest scales of the forced flows deviate from the absolute equilibrium solutions.

DOI: 10.1103/PhysRevFluids.2.114602

I. INTRODUCTION

Experiments and numerical studies [1,2] are known to reproduce, up to intermittency corrections [3], the energy spectrum power law predicted by Kolmogorov's 1941 theory of turbulence [4]: $E(k) \propto \epsilon^{2/3}k^{-5/3}$ where k and ϵ denote the wave number and the energy dissipation respectively. This power law is valid in the inertial range, i.e., for wave numbers satisfying $k_f < k < k_d$ where k_f and $k_d \sim k_f \mathrm{Re}^{3/4}$ denote the forcing wave number and the viscous dissipation wave number respectively. The Reynolds number Re is defined as $\mathrm{Re} \equiv U/\nu k_f$ where U stands for the root mean square velocity and ν denotes the viscosity. In order to maximize the size of this inertial range, most experiments and direct numeric simulations (DNSs) forced the flow at the largest scale of the system. At these scales the dynamics of the system can be described in terms of the Richardson cascade [3] where large scales transfer their energy to smaller scales with large eddies breaking into smaller eddies. This simple description cannot be used to describe the dynamics at scales larger than the forcing scale (from now on referred to as the *large scales*). Indeed, contrary to the inertial range, large scales do not have a direct flux of energy coming from the forcing scale. Some theoretical arguments [3,5,6] indicate that they can be described by the dynamics of absolute equilibrium solutions of the spectrally truncated Euler equation (TEE) given by

$$\partial_t \boldsymbol{u} + \mathbb{P}_{k_M}[\boldsymbol{u} \cdot \boldsymbol{\nabla}\boldsymbol{u} + \boldsymbol{\nabla} P] = 0 \quad \text{and} \quad \boldsymbol{\nabla} \cdot \boldsymbol{u} = 0, \tag{1}$$

where $\boldsymbol{u}$, P, and k_M denote the velocity field, the pressure field, and the truncation wave number, respectively. The operator $\mathbb{P}_{k_M}$ enforces a spherical truncation in the TEE. It acts in Fourier space as a

[*]alexandre.cameron@ens.fr
[†]alexakis@lps.ens.fr
[‡]brachet@physique.ens.fr

small-scale filter. The modes whose wave numbers satisfy $|\boldsymbol{k}| \leqslant k_M$ are unaffected by the projection, whereas the amplitudes of the other modes are all set to zero. Despite keeping the amplitude of the truncated modes to zero, the projection conserves the total energy and helicity of the flows. After a transient state, the system reaches an absolute equilibrium state which has been conjectured to follow a Boltzmann-Gibbs distribution depending only on the initial energy and helicity of the flow. Under these assumptions, Kraichnan [7] predicted the form of the energy and helicity spectrum. DNSs of the TEE performed in Refs. [8,9] verified the absolute equilibrium energy and helicity spectra predicted in Ref. [7].

The TEE (1) needs to be contrasted with the forced Navier-Stokes equation (NSE) that governs the evolution of viscous flows and is given by

$$\partial_t \boldsymbol{u} + (\boldsymbol{u} \cdot \boldsymbol{\nabla})\boldsymbol{u} = -\boldsymbol{\nabla} P + \nu \Delta \boldsymbol{u} + \boldsymbol{F} \quad \text{and} \quad \boldsymbol{\nabla} \cdot \boldsymbol{u} = 0, \tag{2}$$

where $\boldsymbol{u}$, P, and ν denote the velocity field, the pressure field and the viscosity respectively. $\boldsymbol{F}$ denotes the forcing field that is acting at a particular wave number k_f. Note that unlike the TEE, in the NSE, energy needs to be supplied by the forcing term, in order to compensate viscous dissipation. As a result of the presence of viscosity, the solutions of the equation are dependent on the Reynolds number. Furthermore, the energy and helicity of the system at steady state are not determined by the initial conditions as in the TEE, but depend on the forcing, the domain size, and the viscosity. Despite these differences, the large scales could, in principle, be modeled as in the state of absolute equilibrium predicted in Ref. [7] due to the absence of mean flux of energy. Recently, Dallas *et al.* [10] performed turbulent DNSs with enough resolution to model flows with significant scale separation between the forcing scale $\ell_f \propto 1/k_f$ and the domain scale L. In their study, it was reported that large-scale spectra are in agreement with the absolute equilibrium theory, although some deviations at scales of the order of the domain size were reported. Among other reasons, these deviations could be attributed to large-scale instabilities [11,12].

Agreement in the spectra, however, does not guarantee the presence of an absolute equilibrium, since the temporal dynamics can be different. The differences (or the equivalence) between the temporal dynamics of the large scale modes of solution of the NSE and the absolute equilibrium solutions of the TEE have not yet been investigated. Note that the equivalence of the temporal dynamics of the two systems is a much more stringent condition than the simple equivalence of their spatial spectra. The correlation time of the system is a good measurement to asses the temporal dynamics of large-scale modes. It can differ between the Eulerian and Lagrangian frameworks. For instance, in the inertial range, the Lagrangian correlation time is proportional to $k^{-2/3}$ because of Kolmogorov's scaling, whereas the Eulerian correlation time in proportional to k^{-1} [13] because of the swiping effect. In pseudospectral DNSs, the Eulerian correlation time of the modes of the velocity field is the best suited to describe the temporal dynamics of the system. Numerical solutions have already been used to analyze the temporal evolution of statistical equilibrium in the statistically stationary regime without helicity in Ref. [8] and in the transitory regime with helicity in Ref. [9]. But the characterization of the correlation time and comparison with the large scales of the NSE has not yet been performed.

The aim of the present paper is to compare the statistics of individual modes and the temporal properties of the TEE solutions and those of the large scales of the NSE. In Sec. II we review absolute equilibrium theory and derive analytic results for the correlation time of incompressible flows solutions of the TEE for arbitrary helicity. In Sec. III we validate these predictions with numerical solutions of the TEE, and in Sec. IV we test if they also apply to the large scales of solutions of the NSE for different forcing functions. Our conclusions are drawn in the last section.

II. ABSOLUTE EQUILIBRIUM AND THERMALIZATION THEORY

A. Energy and helicity spectra

The derivation of absolute equilibrium statistics for helical flows was carried out by Kraichnan [7,14] in an analogy to microcanonical ensembles in statistical thermodynamics [15]. Similarly to

the microcanonical ensemble, the TEE conserves the total energy, E. In addition, the TEE also conserves the total helicity, H, which is another global quadratic quantity in velocity

$$E = \frac{1}{2}\frac{1}{L^3}\int |\boldsymbol{u}|^2 d\boldsymbol{r}, \quad H = \frac{1}{2}\frac{1}{L^3}\int \boldsymbol{u}\cdot\boldsymbol{\omega} d\boldsymbol{r}, \tag{3}$$

where $L^3 = \int d\boldsymbol{r}$ and $\boldsymbol{\omega} = \boldsymbol{\nabla}\times\boldsymbol{u}$.

In analogy with the thermodynamic canonical ensemble, in a statistically steady state, absolute equilibrium solutions of the TEE will correspond to a flow in a state $\boldsymbol{u}$ with probability $\mathcal{P}(\boldsymbol{u})$ that follows the Boltzmann-Gibbs distribution

$$\mathcal{P}(\boldsymbol{u}) = \frac{1}{Z}e^{-\mathcal{C}(\boldsymbol{u})}. \tag{4}$$

The functional $\mathcal{C}(\boldsymbol{u})$ is a linear combination of the energy E and the helicity H of the flow

$$\mathcal{C}(\boldsymbol{u}) = \alpha E + \beta H = \alpha\left(E - \mathrm{Kr}\frac{H}{k_M}\right) \quad \text{and} \quad \mathrm{Kr} = -\frac{\beta k_M}{\alpha}, \tag{5}$$

where α and β are two parameters introduced by Kraichnan and k_M is the truncation wave number introduced in Eq. (1). These parameters unequivocally define a class of absolute equilibrium solutions of the TEE with a fixed energy E and helicity H. What we presently call the Kraichnan number Kr is a dimensionless combination of α, β, and k_M. The Kraichnan number indicates the degree of helicity of the flow. When $\mathrm{Kr} = 0$, the flow does not have helicity, whereas when $|\mathrm{Kr}| = 1$ the flow is maximally helical. As of consequence of the definition of $\mathcal{C}(\boldsymbol{u})$, velocity modes are independent Gaussian variables. The partition function Z used as normalization in Eq. (4) is defined by

$$Z = \int \mathcal{D}\boldsymbol{u} e^{-\mathcal{C}(\boldsymbol{u})}. \tag{6}$$

Similarly to statistical thermodynamics, Boltzmann-Gibbs weights can be used to compute statistical averages over the space of incompressible flows. The average of a generic observable $f(\boldsymbol{u})$ is then given by

$$\langle f(\boldsymbol{u})\rangle = \frac{1}{Z}\int \mathcal{D}\boldsymbol{u} f(\boldsymbol{u}) e^{-\mathcal{C}(\boldsymbol{u})}. \tag{7}$$

In the case of the TEE, the truncation in wave number implies that the functional integral can be done over a finite number of Fourier modes $\widetilde{\boldsymbol{u}}_{\boldsymbol{k}}$ that satisfy the incompressibility condition $\boldsymbol{k}\cdot\widetilde{\boldsymbol{u}}_{\boldsymbol{k}} = 0$. This last condition can be simplified by using the Craya-Herring-Lesieur [16–18] helical decomposition. Each Fourier mode $\widetilde{\boldsymbol{u}}_{\boldsymbol{k}}$ is written as the sum of two modes of opposite helicity which belongs to the Craya-Herring-Lesieur plane, $\widetilde{\boldsymbol{u}}_{\boldsymbol{k}} = \widetilde{\boldsymbol{u}}^{+}_{\boldsymbol{k}} + \widetilde{\boldsymbol{u}}^{-}_{\boldsymbol{k}}$, where

$$\widetilde{\boldsymbol{u}}^{\pm}_{\boldsymbol{k}} = \frac{1}{2}\left[\widetilde{\boldsymbol{u}}_{\boldsymbol{k}} \pm \frac{\widetilde{\boldsymbol{\omega}}_{\boldsymbol{k}}}{k}\right] \tag{8}$$

with $\widetilde{\boldsymbol{\omega}}_{\boldsymbol{k}} = i\boldsymbol{k}\times\widetilde{\boldsymbol{u}}_{\boldsymbol{k}}$. This leads to two independent complex amplitudes $\widetilde{\boldsymbol{u}}^{\pm}_{\boldsymbol{k}}$ for each Fourier mode of an incompressible flow. Using this statistical average of Eq. (7), the average energy and helicity of the modes of the flow can be derived analytically. Since the PDF of every mode of the velocity field follows a Gaussian distribution, the average energy $\langle e_{\boldsymbol{k}}\rangle = \frac{1}{2}\langle|\widetilde{\boldsymbol{u}}_{\boldsymbol{k}}|^2\rangle$ and average helicity $\langle h_{\boldsymbol{k}}\rangle = \frac{1}{2}\langle\widetilde{\boldsymbol{u}}_{-\boldsymbol{k}}\cdot\widetilde{\boldsymbol{\omega}}_{\boldsymbol{k}}\rangle$ of each wave vector are given by

$$\langle e_{\boldsymbol{k}}\rangle = \frac{\alpha^{-1}}{1-\left(\mathrm{Kr}\frac{k}{k_M}\right)^2} \quad \text{and} \quad \langle h_{\boldsymbol{k}}\rangle = \frac{\beta}{\alpha}\frac{\alpha^{-1}k^2}{1-\left(\mathrm{Kr}\frac{k}{k_M}\right)^2} = \frac{\beta}{\alpha}k^2\langle e_{\boldsymbol{k}}\rangle. \tag{9}$$

When $|\mathrm{Kr}| \to 1$, the energy is confined in the modes in the smallest scales of wave number near k_M.

The absolute equilibrium distribution can be expressed using the Craya-Herring-Lesieur [16–18] helical decomposition for the energies $\langle e_{\boldsymbol{k}}^{\pm}\rangle = \frac{1}{2}\langle|\tilde{\boldsymbol{u}}_{\boldsymbol{k}}^{\pm}|^2\rangle$ and helicities $\langle h_{\boldsymbol{k}}^{\pm}\rangle = \pm k\langle e_{\boldsymbol{k}}^{\pm}\rangle$:

$$\langle e_{\boldsymbol{k}}^{\pm}\rangle = \frac{1}{2}\frac{\alpha^{-1}}{1-(\pm)\mathrm{Kr}\frac{k}{k_M}} \quad \text{and} \quad \langle h_{\boldsymbol{k}}^{\pm}\rangle = \frac{1}{2}\frac{\pm\alpha^{-1}k}{1-(\pm)\mathrm{Kr}\frac{k}{k_M}}. \tag{10}$$

When $\mathrm{Kr} \to 1$, the energy is confined in the small scale modes and more precisely in their positive helical components. The energy spectra are then obtained by spherically averaging over all modes of the same modulus

$$E^{\pm}(k) \equiv \sum_{|\boldsymbol{k}|=k}\langle e_{\boldsymbol{k}}^{\pm}\rangle \simeq \frac{2\pi k^2\alpha^{-1}}{1-(\pm)\mathrm{Kr}\frac{k}{k_M}} \quad \text{and} \quad E(k) = E^{+}(k) + E^{-}(k) \simeq \frac{4\pi k^2\alpha^{-1}}{1-\left(\mathrm{Kr}\frac{k}{k_M}\right)^2} \tag{11}$$

and similarly for the helicity spectra

$$H^{\pm}(k) \equiv \sum_{|\boldsymbol{k}|=k}\langle h_{\boldsymbol{k}}^{\pm}\rangle \simeq \frac{\pm 2\pi k^3\alpha^{-1}}{1-(\pm)\mathrm{Kr}\frac{k}{k_M}} \quad \text{and} \quad H(k) = H^{+}(k) + H^{-}(k) \simeq \frac{4\pi k^4\alpha^{-2}\beta}{1-\left(\mathrm{Kr}\frac{k}{k_M}\right)^2}. \tag{12}$$

B. Correlation times of absolute equilibrium solutions

The derivations so far predict the ensemble average of the energy and helicity per mode. However, they do not characterize the temporal properties of the system. The computation of the spectra requires only the knowledge of the conserved quantities of the TEE and not the equation itself. To describe with more depth the properties of the solutions of the TEE or the NSE in the thermalization domain, the temporal properties of the flows must be analyzed.

In Ref. [8] Cichowlas *et al.* studied the correlation time of absolute equilibrium solutions of the TEE without helicity. It was shown that the correlation time $\tau_{\boldsymbol{k}}^{E}$ [defined more precisely below: Eq. (17)] depends on the energy E of the flow and is inversely proportional to the wave number $\boldsymbol{k}$

$$\tau_{\boldsymbol{k}}^{E} \propto k^{-1}E^{-1/2}. \tag{13}$$

The k^{-1} scaling law is similar to that of the swiping effect, although we note that the swiping effect argument cannot be applied since the absolute equilibrium energy is not concentrated in the largest scale. In this present work, we extend this result for flows with an arbitrary helicity and show that a new power law emerges when the flow is strongly helical. This new power law depends on the helicity H of the flow rather than the energy and reads

$$\tau_{\boldsymbol{k}}^{H} \propto k^{-1/2}H^{-1/2}. \tag{14}$$

This new power law is valid for highly helical flows and wave numbers in the range $k_c \ll k \ll k_M$ where $k_c \propto k_M(1-|\mathrm{Kr}|)\ln(1-|\mathrm{Kr}|)$, while the nonhelical scaling law of Eq. (13) is valid for $k \ll k_c$. In what follows, we give a sketch of the derivation of Eqs. (13) and (14), and the full derivation is presented in the Appendixes.

The correlation time will be built using the short time approximation of the correlation function. The temporal correlation function $\Gamma_{\boldsymbol{k}}(t)$ of a mode is defined as

$$\Gamma_{\boldsymbol{k}}(t) = \frac{\overline{\boldsymbol{u}_{\boldsymbol{k}}^{*}(s)\boldsymbol{u}_{\boldsymbol{k}}(s+t)}}{\overline{|\boldsymbol{u}_{\boldsymbol{k}}(s)|^2}} \quad \text{where} \quad \overline{f(s)} = \lim_{T\to\infty}\frac{1}{2T}\int_{-T}^{T} f(s)\,ds. \tag{15}$$

It satisfies the relations $\Gamma_{\boldsymbol{k}}(0) = 1$ and $\Gamma_{\boldsymbol{k}}(t) = \Gamma_{\boldsymbol{k}}(-t)$. If the system loses memory as time elapses, the correlation function also satisfies $\Gamma_{\boldsymbol{k}}(\infty) = 0$. Thus, the correlation function assesses how fast a mode decorrelates from its initial value. Using the Taylor expansion of the correlation function near $t = 0$, the correlation function can be written as

$$\Gamma_{\boldsymbol{k}}(t) = 1 - \frac{1}{2}t^2\tau_{\boldsymbol{k}}^{-2} + \cdots \quad \text{with} \quad \tau_{\boldsymbol{k}}^{-2} = -\partial_t^2\Gamma_{\boldsymbol{k}}|_{t=0} = -\frac{\overline{\boldsymbol{u}_{\boldsymbol{k}}^{*}(s)\partial_t^2\boldsymbol{u}_{\boldsymbol{k}}(s+t)}|_{t=0}}{\overline{|\boldsymbol{u}_{\boldsymbol{k}}(s)|^2}}, \tag{16}$$

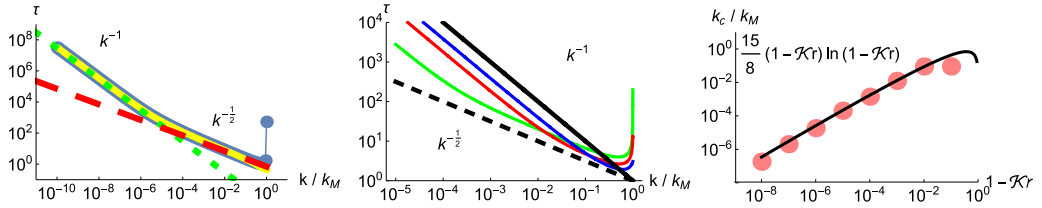

FIG. 1. (Left) Correlation time as a function of the wave number for $1 - \mathrm{Kr} = 10^{-6}$. The results are represented with the full line with dark dots for the positive helical components and in bright dots for the negative helical components. The $k^{-1/2}$ scaling law is represented with the dashed line. The k^{-1} scaling law is represented with the dotted line. (Center) Dependence of the correlation time for the positive helical component. The Kraichnan number is increased at fixed energy: $\mathrm{Kr} \in \{1 - 10^{-1}; 1 - 10^{-2}; 1 - 10^{-4}\}$, represented by blue, red, and green lines, respectively. The dotted line represents the $k^{-\frac{1}{2}}$ scaling law, and the full line represents the k^{-1} scaling law. (Right) Transition wave number as a function of $1 - \mathrm{Kr}$, the semianalytic prediction is represented with dots, and the $\frac{15}{8}(1 - \mathrm{Kr})\ln(1 - \mathrm{Kr})$ scaling law is represented with the full line.

where $\tau_{\boldsymbol{k}}$ will be referred to as the parabolic correlation time. The term $-\overline{\boldsymbol{u}_{\boldsymbol{k}}^*(s)\partial_t^2\boldsymbol{u}_{\boldsymbol{k}}(s+t)}|_{t=0}$ can be rewritten as $\overline{|\partial_t\boldsymbol{u}_{\boldsymbol{k}}(s+t)|^2}_{t=0}$ using an integration by parts. Assuming that the TEE system is ergodic, the averages over time can be replaced by the statistical averages defined in Eq. (7). The correlation time can then be expressed as

$$\tau_{\boldsymbol{k}} = \sqrt{\frac{\langle|\boldsymbol{u}_{\boldsymbol{k}}|^2\rangle}{\langle|\partial_t\boldsymbol{u}_{\boldsymbol{k}}|^2\rangle}}. \tag{17}$$

The expression of $\langle|\boldsymbol{u}_{\boldsymbol{k}}|^2\rangle$ is given by the absolute equilibrium statistics. On the other hand, the expression of $\langle|\partial_t\boldsymbol{u}_{\boldsymbol{k}}|^2\rangle$ can be computed using the temporal evolution equation of the mode given by Eq. (1) in the case of the TEE. The property that the modes of the velocity field are independent Gaussian variables is used to compute the averages.

In the limit where $\mathrm{Kr} \to 1$ and $k/k_M \to 0$, it is possible to compute an asymptotic expression of the correlation time with the Craya-Herring-Lesieur helical decomposition [16–18] (see the appendixes). In this limit, most of the energy is concentrated in the positive helical components of the modes near k_M. The interactions of these modes are the dominant terms in the temporal evolution equation and give a theoretical prediction for the correlation time

$$\tau_{\boldsymbol{k}} \simeq \sqrt{\frac{\langle|\boldsymbol{u}_{\boldsymbol{k}}^+|^2\rangle}{\langle|\partial_t\boldsymbol{u}_{\boldsymbol{k}}^+|^2\rangle}} \underset{\substack{\mathrm{Kr}\to 1\\ k/k_M\to 0}}{=} \sqrt{\frac{\frac{15}{8}(1-\mathrm{Kr}) - \frac{k}{k_M\ln(1-\mathrm{Kr})}}{4\pi\alpha^{-1}k^2\left(1 - s_{\boldsymbol{k}}\mathrm{Kr}\frac{k}{k_M}\right)}} \quad \text{with} \quad \alpha = \frac{\tanh^{-1}(\mathrm{Kr}) - \mathrm{Kr}}{2E_{\mathrm{tot}}\mathrm{Kr}^3}. \tag{18}$$

The left panel of Fig. 1 represents the correlation time τ_k as a function of k for a Kraichnan number near one: $\mathrm{Kr} = 1 - 10^{-6}$. Both power laws k^{-1} and $k^{-1/2}$ are represented. The k^{-1} power law is valid in the largest wave numbers, $k \ll k_c$, while the $k^{-1/2}$ power law is valid for an intermediate range of wave number: $k_c \ll k \ll k_M$. The center panel of Fig. 1 represents the dependence of the correlation time at different Kraichnan numbers for fixed total energy E_{tot}. As $\mathrm{Kr} \to 1$, the correlation time in the small scales increases, and the correlation time in the large scales decreases. For absolute equilibrium solutions of the TEE, increasing the helicity slows the dynamics of the small scales and makes the dynamics of the large scales more rapid. The right panel of Fig. 1 represents the dependence of the transition wave number k_c with $1 - \mathrm{Kr}$. The value of the transition wave number was estimated using the intersection of the two power laws. The dark curve on the graph indicates that the critical wave number follows closely the $A(1 - \mathrm{Kr})\ln(1 - \mathrm{Kr})$ prediction. Even though helicity does not appear explicitly in Eq. (18), the correlation time has a $k^{-\frac{1}{2}}$ scaling for intermediate wave numbers when $1 - \mathrm{Kr} \ll k/k_M \ll 1$. This scaling is similar to the helicity-based correlation

time [see Eq. (14)] and appears for a range of Kraichnan numbers corresponding to highly helical flows.

III. TRUNCATED EULER DNS

In the previous section, we discussed some predictions on the properties of the PDF, the standard derivation and the correlation time of solutions of the TEE. We will now check their validity in periodic flows with and without Taylor-Green (TG) symmetries [19]. The DNSs with TG symmetries were performed using the pseudospectral code TYGRES [20], and those without TG symmetries were performed using the pseudospectral code GHOST [21,22]. The major advantage of studying flows with TG symmetries is that the symmetries can be used to gain a factor 32 in both storage and execution time. However, flows with TG symmetries have a total helicity equal to zero and consequently always have a Kraichnan number equal to zero. In order to study helical flows, DNSs have to be performed in the general-periodic domain without TG symmetry. This last configuration will be referred to as general-periodic flow in opposition to TG symmetric flows.

A. No helicity: Inviscid Taylor-Green flows

The first flows used to probe the statistical properties of the TEE have TG symmetries that impose the total helicity to be equal to zero. As a consequence of TG symmetries [23], the Fourier expansion of the flow can be expressed with the following simplified expression:

$$\begin{bmatrix} u_{\boldsymbol{r}}^x \\ u_{\boldsymbol{r}}^y \\ u_{\boldsymbol{r}}^z \end{bmatrix} = \sum_{k_x=0}^{\infty}\sum_{k_y=0}^{\infty}\sum_{k_z=0}^{\infty} \begin{bmatrix} u_{\boldsymbol{k}}^x \times \sin k_x x & \cos k_y y & \cos k_z z \\ u_{\boldsymbol{k}}^y \times \cos k_x x & \sin k_y y & \cos k_z z \\ u_{\boldsymbol{k}}^z \times \cos k_x x & \cos k_y y & \sin k_z z \end{bmatrix}, \tag{19}$$

where $\boldsymbol{u_k} \in \mathbb{R}^3$ if k_x, k_y, k_z are all odd or all even integers and $\boldsymbol{u_k} = 0$ otherwise. All the properties of the Fourier coefficients related to TG symmetries can be found in the appendix of Ref. [23]. Specific properties useful to understand the number of independent variables of TG symmetric flows are presented in the Appendixes.

Incompressible random flows with TG symmetries and energy equipartition were used to initialize the simulations. Since TG symmetric flows do not have helicity ($H = 0$ and $\mathrm{Kr} = 0$), the thermalization theory of Sec. II B predicts that they should follow

$$\langle e_{\boldsymbol{k}} \rangle = \alpha^{-1} \quad \text{thus} \quad E(k) = \frac{4\pi k^2}{{k_M}^3}\alpha^{-1} \quad \text{and} \quad \tau_{\boldsymbol{k}} \underset{k/k_M \to 0}{=} \sqrt{\frac{45\alpha}{112}}\frac{1}{k}. \tag{20}$$

The first hypothesis in the absolute equilibrium theory is that the components of velocity are independent Gaussian variables. As detailed in the appendixes, in TG flows, the even modes with one of their components equal to zero—i.e., of the form $(0,k_y,k_z)$, $(k_x,0,k_z)$, or $(k_x,k_y,0)$—and the xy diagonal modes—i.e., of the form $(k_\perp,k_\perp,k_\parallel)$—both have only one degree of freedom corresponding to their real amplitude. All other TG modes have two degrees of freedom. To test this assumption, temporal series of the modes are recorded and analyzed to extract the PDF. PDFs of modes with one degree of freedom are presented in the left panel of the Fig. 2 at different wave numbers. On the semilogarithmic scale, the distributions of the modes follow the parabolic trend characteristic of a Gaussian distribution. The right panel of Fig. 2 represents the distribution of energy of the different velocity modes. By definition, the energy is the sum of the square of the velocity components. If at a particular wave number $\boldsymbol{k}$ there are g modes that are independent and Gaussian, then the distribution of the energy $e_{\boldsymbol{k}}$ that lies at that wave number must follow a χ_g^2 distribution [24]

$$\chi_g^2(e_{\boldsymbol{k}}) = \frac{1}{2^{\frac{g}{2}}\Gamma\left(\frac{g}{2}\right)}(e_{\boldsymbol{k}})^{\frac{g}{2}-1}\exp\left[-\frac{e_{\boldsymbol{k}}}{2}\right], \tag{21}$$

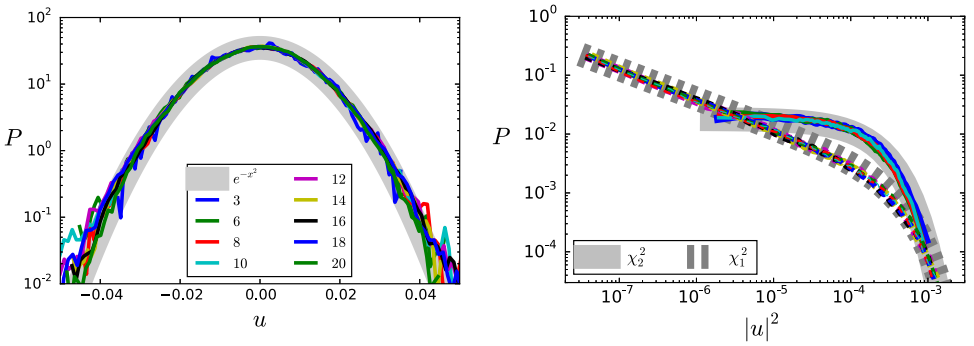

FIG. 2. (Left) PDF of the amplitude of the velocity of modes with one degree of freedom of Taylor-Green symmetric DNSs in semilogarithmic scale. The color of the thin lines indicates the wave number of the mode as described in the legend box of the plot. (Right) PDF of energy of the modes of Taylor-Green symmetric DNSs of the truncated Euler equation in logarithmic scale: (thick) theoretical predictions, (thin dashed) one degree of freedom, (thin full) two degrees of freedom. The χ_1^2 and χ_2^2 plots are drawn using the formula presented in Eq. (21).

where g denotes the number of independent Gaussian variables (see the appendixes). Thus, the power law behavior at small values of $e_{\boldsymbol{k}}$ reveals the degrees of freedom involved. Due to the symmetries of the TG flows, different wave numbers have different degrees of freedom. The modes—$(0,k_y,k_z)$, $(k_x,0,k_z)$, $(k_x,k_y,0)$, and $(k_\perp,k_\perp,k_\parallel)$—have one degree of freedom and should have an energy distribution following a χ_1^2 law. All other modes have two degrees of freedom and have an energy distribution following a χ_2^2 law. If the energy follows a χ^2 distribution, it does not necessarily imply that the velocity has a Gaussian statistics, it is only a characteristic of the sum of Gaussian distributions. However, we will check only the Gaussian statistics of modes with one degree of freedom and look at the energy distribution of the other modes.

To check the equipartition of the energy, the standard deviation of modes can be computed with their temporal series, or the energy of all the modes within a shell of constant wave numbers can be summed. The first method can be performed with the same temporal series used to plot the PDF of the modes in Fig. 2. Using this time average, the standard deviation, $\sigma^2 = \langle e_k \rangle$, is represented in the left panel of Fig. 3. The second method, with the shell-summed energy at a fixed time, is presented in the right panel of Fig. 3. If the system satisfies energy equipartition and is ergodic, the amount of

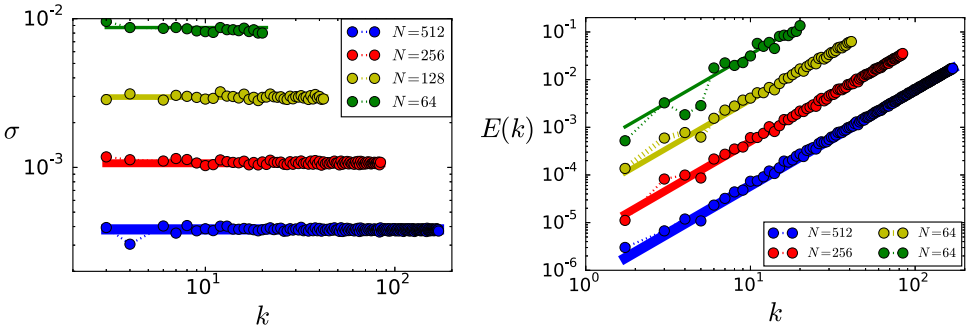

FIG. 3. (Left) Average standard deviation of the velocity, σ, of Taylor-Green symmetric DNSs of the truncated Euler equation for different resolutions. (Right) Energy spectrum, $E(k)$, of Taylor-Green symmetric DNSs of the truncated Euler equation at different resolutions $N = \{64, 128, 256, 512\}$ for a fixed energy. The results are consistent with the theoretical prediction that $E(k) \sim 4\pi k^2 \sigma^2$. In both plots, the numeric data are represented with dots and the theoretical prediction with full lines.

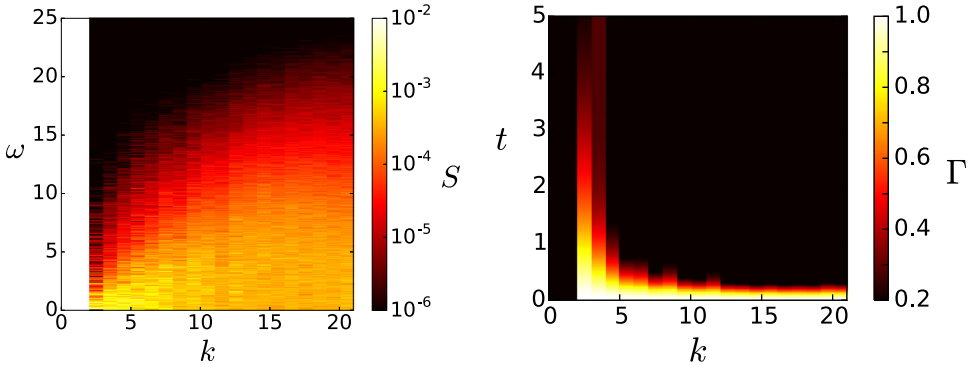

FIG. 4. Spatio-temporal spectrum of Taylor-Green symmetric DNSs of the truncated Euler equation. (Left) Power spectrum $S(k,\omega)$. (Right) Correlation function $\Gamma(k,t)$.

energy per shell should be proportional to the surface of the shell, $4\pi k^2$. This is shown in the right panel where $E(k)$ is plotted. The differences at low k are due to sampling error.

1. Correlation time computation

The temporal statistics of the modes depend on the evolution equation and not only on the conserved quantities. Since the correlation function and consequently the correlation time are specific properties of the evolution equation, their measurement characterizes the temporal evolution of the system. In order to compute the correlation function and assess the correlation time, we developed a method similar to that used to produce spatio-temporal spectrum in wave experiments [13,25,26], where the spatio-spectral spectrum $S(k,\omega)$ is first calculated and the correlation function $\Gamma(k,t)$ is obtained by a Fourier transform using the Wiener-Khinchin theorem [27]. This method is explained in the appendices.

Figure 4 presents in the left panel the spatio-temporal color plot of the power spectrum $S(k,\omega)$ and in the right panel the correlation function $\Gamma(k,t)$.

The correlation functions for different velocity modes are shown in the left panel of Fig. 5. The time of each correlation function has been rescaled by the correlation time measured. As shown in the left panel of Fig. 5, the correlation functions collapse on the same curve for times in the range $0 \leqslant t \leqslant \tau_k$. Since long time series are required for the correlation function to converge at long times, the curves collapse only for $t < \tau_k$. This collapse at small time confirms that the parabolic assumption made in Eq. (17) is valid for absolute equilibrium solutions of the TEE. Furthermore, the good agreement of

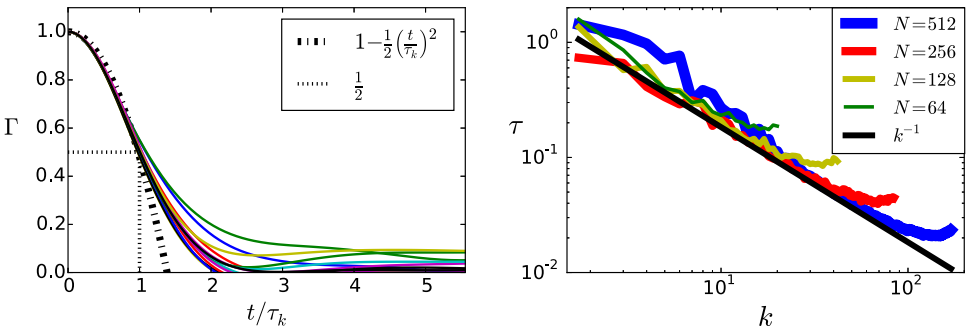

FIG. 5. Temporal correlation properties of Taylor-Green symmetric DNSs of the truncated Euler equation. (Left) Correlation function as a function of time. (Right) Correlation time as a function of wave number. The k^{-1} power law is plotted with the normalization deriving from Eq. (20).

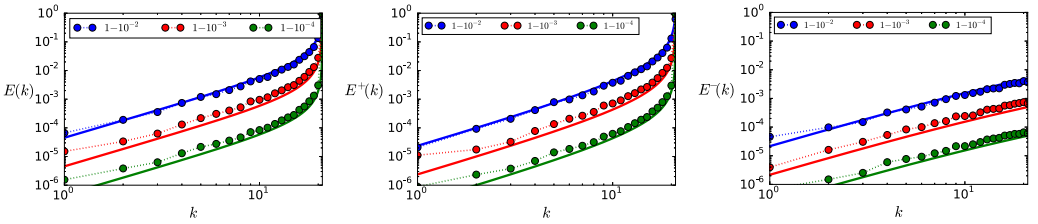

FIG. 6. Energy spectrum for different Kraichnan numbers $\mathrm{Kr} \in \{1-10^{-2}; 1-10^{-3}; 1-10^{-4}\}$ for general-periodic solutions of the truncated Euler equation. The numeric data are represented with dots and the theoretical prediction of Eq. (11) with full lines. (Left) Energy spectrum associated to the total velocity. (Center) Energy spectrum associated to the positive helical component of the velocity. (Right) Energy spectrum associated to the negative helical component of the velocity. In both panels, the full lines are associated with the energy of the total velocity; the dotted lines are associated with the energy of the positive helical component of the velocity; and the dashed lines are associated with the energy of the negative helical component of velocity.

the curve until τ_k also confirms that the half-height time is a good proxy to measure the correlation time. The right panel of Fig. 5 represents the correlation time of an absolute equilibrium solution of the TEE. The correlation time computed using the numerical data is consistent with the k^{-1} scaling law characteristic of an energy-based correlation time. The thermodynamic model developed in the previous section is therefore in agreement with the measurements carried out with TG symmetric DNSs.

B. Inviscid flows with helicity

The next set of DNSs of the TEE were carried out using the pseudospectral code GHOST [21,22]. In these DNSs, for every wave number four real degrees of freedom exist. Indeed, the Craya-Herring-Lesieur helical decomposition [16–18] states that every Fourier mode of velocity can be separated into a positive and a negative helical component as expressed in Eq. (10). The two helical components are modulated by their complex amplitude. Since there is no additional restriction on the amplitude of the mode, the velocity modes have four real degrees of freedom.

All flows are initialized with the same energy but with different helicity, determined using the the Kraichan number $\mathrm{Kr} = -k_M\beta/\alpha$. This parameter is not present for the TG flows and leads to major differences in the global aspect of the PDF of the modes. For the same wave number, the helical components of helical flows have different energies.

Figure 6 represents the energy spectrum of the highly helical flows $\mathrm{Kr} = \{1-10^{-2}; 1-10^{-3}; 1-10^{-4}\}$. The results in the left panel come from DNSs, and those in the right panel are from the absolute equilibrium theory [7]. Theoretical and numerical results match, which confirms the validity of absolute equilibrium theory.

Figure 7 presents the PDF of the helical components of the velocity of two general-periodic flows with different Kraichnan numbers. The first flow has a Kraichnan number of zero and consequently does not have any helicity. The second flow has a Kraichnan number of 0.9 and is thus highly helical. For every wave number and every Kraichnan number, the energy of the positive and negative helical components of the velocity follows a χ_2^2 distribution. The χ_2^2 distribution is characteristic of the sum of the square of two independent Gaussian variables. The hypothesis of Gaussian-distributed velocity modes is therefore in agreement with the DNSs. The PDFs of the positive and negative helical modes at $k = k_M$ collapse for the nonhelical flow at $\mathrm{Kr} = 0$ but do not collapse for the highly helical flow at $\mathrm{Kr} = 0.9$. The separation of the PDFs at $\mathrm{Kr} = 0.9$ is consistent with the statistics presented in Eq. (10). All the characteristics of the energy distribution of the DNSs are in good agreement with the properties predicted by the absolute equilibrium theory.

The last property that will be examined concerns the evolution of the correlation time as the flow becomes highly helical ($\mathrm{Kr} \to 1$). The thermalization theory, presented in Sec. II, predicts that, as the

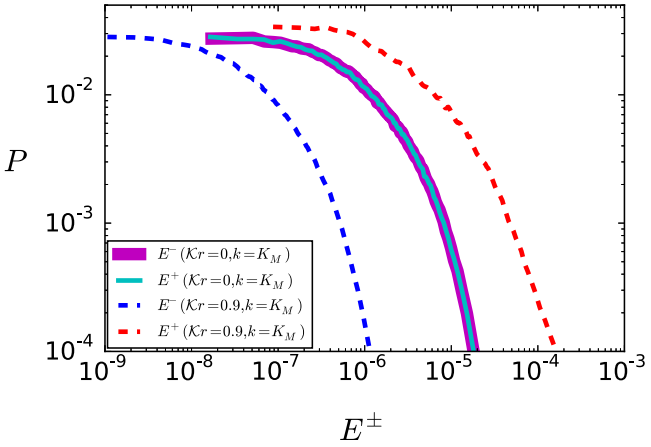

FIG. 7. Separation of the PDFs due to helicity in solutions of the truncated Euler equation. The PDFs have been rescaled to plateau at the same level near zero in order to compare the width of the tail of the distribution at large values. At $k = k_M$, the distributions of probability have an offset for Kr $= 0.9$ because helicity greatly affects the distribution of energy in the small scales.

system becomes highly helical, the energy-based correlation time [τ_k^E in Eq. (13)] should transition to a helicity-based correlation time [τ_k^H in Eq. (14)] in intermediate scales $(1 - \mathrm{Kr}) \ll k/k_M \ll 1$. With the current computational power, it is difficult to show the same number of orders of magnitude as in Fig. 1. Consequently, the results presented in Fig. 8 are not able to show both scaling laws for a given Kr. The left panel of Fig. 8 presents the correlation time of a nonhelical flow at Kr $= 0$ while the right panel of Fig. 8 presents the correlation time of a highly helical flow at Kr $= 0.9$. The correlation time of the nonhelical flow exhibits a k^{-1} scaling law characteristic of an energy-based correlation time, while the correlation time of the highly helical flow is closer to a $k^{-\frac{1}{2}}$ scaling law characteristic of a helicity-based correlation time. For Kr $= 0.85$, the power law appears to take an intermediate exponent, however, as the theoretical results of Sec. II B predict that this is a transient effect and a behavior closer to Fig. 1 is expected at larger scale separation.

Additionally, in the right panel of Fig. 8, the correlation time peaks in the small scales, which is characteristic of the localization of the energy near k_M of helical flows. In the highly helical case, the difference between the positive and negative helical components of the velocity can also be observed in the small scales. While both helical components collapse in the nonhelical case, they are

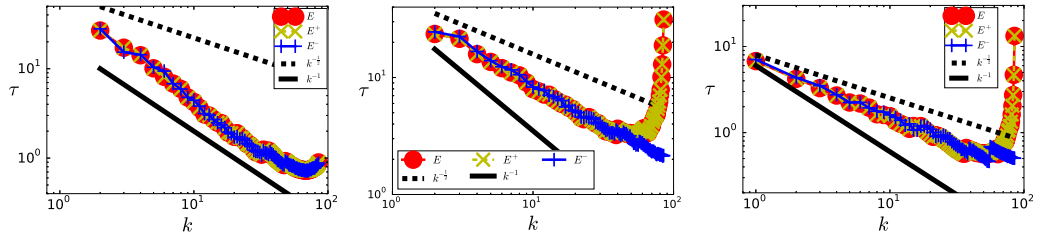

FIG. 8. Correlation time of DNSs of general-periodic solutions of the truncated Euler equation for three Kraichnan numbers. The red dots represent the correlation time computed using the total velocity field, the yellow X crosses and the blue + crosses represent the correlation time computed using the positive and negative components of the helical decomposition, respectively. The black dashed line and full black line represent the $k^{-\frac{1}{2}}$ and k^{-1} power laws, respectively. (Left) Nonhelical flow Kr $= 0$. (Center) Slightly helical flow Kr $= 0.85$. (Right) Highly helical flow Kr $= 0.9$,

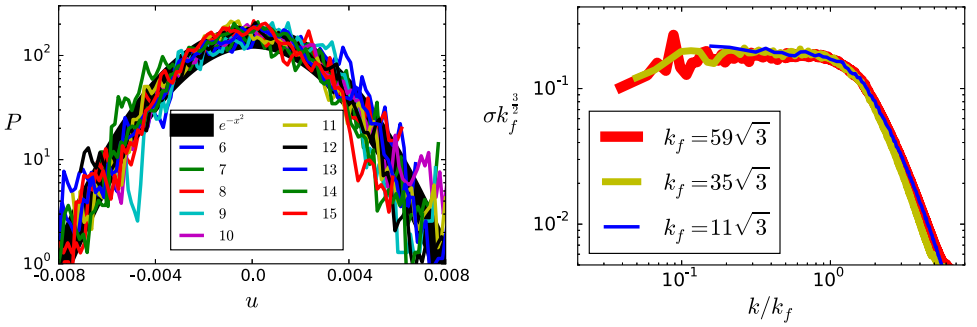

FIG. 9. PDF of modes of Taylor-Green symmetric DNSs of the forced Navier-Stokes equation with a forcing wave number at $k_f = 11\sqrt{3}$. (Left) PDF of even modes with one degree of freedom at scales larger than the forcing scale. (Right) Standard deviation of the velocity modes. As the total energy is constant in the different DNSs, a $k_f^{3/2}$ normalization factor has been introduced in the plot to take into account the increase of the number of modes in the scales larger than the forcing scale.

different in the small scales in the highly helical case. All these observations are in agreement with the correlation time predicted by the thermalization theory. DNSs were also performed at higher Kraichnan numbers and showed a persistence of the helicity-based correlation time.

Even though the transition of the scaling law is hard to observe in the DNSs carried out, results indicate that the transition of correlation time regime occurs for Kraichnan numbers in the range $0.8 \leqslant \mathrm{Kr} \leqslant 0.9$. The center panel of Fig. 8 shows that for slightly less helical flows with $\mathrm{Kr} = 0.85$ the correlation follows a power law with an exponent between -1 and $-\frac{1}{2}$. A clear visualization of the transition is demanding in computational power, since it occurs on nearly one order of magnitude in the left panel of Fig. 1.

IV. NAVIER-STOKES DNS

Because DNSs of the NSE must have a converged spectrum at wave numbers larger than the forcing wave number, their properties cannot be assessed with scale separations as large as those of DNSs of the TEE. Using the same codes as in the previous section, we now turn to the study of how the PDF, the standard deviation and the correlation time behave in the large scales for DNSs of the NSE. We will also compare these results with the observations made on DNSs of the TEE.

A. No helicity: Taylor-Green flows

TG flows are studied with different forcing wave numbers $k_f \in \{11\sqrt{3}; 35\sqrt{3}; 59\sqrt{3}\}$. The forcing was imposed on the flow by fixing to 0.125 the amplitude of the odd modes $[k_f, k_f, k_f]/\sqrt{3}$. The other parameter of the system is the viscosity ν which was also adjusted to reach a turbulent regime. To compare the properties of flows at different forcing wave numbers, the Reynolds number $\mathrm{Re} = U/(\nu k_f)$ was set to 6.56.

Figure 9 represents some properties of the PDF of velocity modes with one degree of freedom in the six planes $k_x \in \{0; 1\}$, $k_y \in \{0; 1\}$, or $k_z \in \{0; 1\}$. These PDFs have a clear Gaussian behavior as highlighted by their parabolic shape on the semilogarithmic plot in the left panel of Fig. 9. The data sets in the left panel, representing modes with $k < k_f$, collapse on the same curve, which indicates that their standard deviation is identical. These two trends are also observed in the right panel of Fig. 9, where the standard deviation of the PDFs are represented for different forcing scales. In the right panel of Fig. 9, the standard deviations, σ, are compensated by a factor $k_f^{3/2}$ to take into account that the total energy is spread out on more modes as the forcing wave number increases. The wave number is also rescaled by the forcing wave number in order to compare the results. Using this scaling, the data sets at different resolutions collapse on the same curve. At large scales,

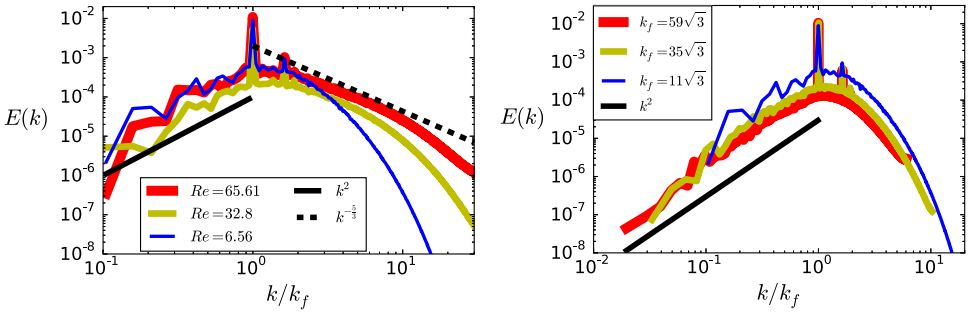

FIG. 10. Energy spectrum of Taylor-Green symmetric flows solutions of the forced Navier-Stokes equation. (Left) Fixed forcing mode $k_f = 11\sqrt{3}$ at different Reynolds numbers Re $\in \{11\sqrt{3}; 35\sqrt{3}; 59\sqrt{3}\}$. (Right) Fixed Reynolds number Re $= 6.56$ at different forcing modes $k_f \in \{11\sqrt{3}; 35\sqrt{3}; 59\sqrt{3}\}$.

the compensated standard deviation plateaus, indicating an analog of the equipartition in energy of absolute equilibrium without helicity Kr $= 0$. Below the forcing scale, the standard deviation rapidly decreases because of the forward cascade and viscosity.

Energy equipartition in the large scale modes can directly be observed in the right panel of Fig. 9. It can also indirectly be observed in the energy spectrum presented in Fig. 10. Since energy shells contain a number of modes proportional to their surface, $4\pi k^2$, systems satisfying equipartition in energy should have an energy spectrum proportional to k^2. The spectra presented on both panels of Fig. 10 are thus consistent with equipartition in energy. In left panel of Fig. 10, the energy spectrum is presented at different Reynolds numbers for a fixed forcing wave number $k_f = 11\sqrt{3}$. At the largest Reynolds number, the energy spectrum reaches the Kolmogorov's $k^{-5/3}$ scaling in the inertial range and has also the equipartition k^2 scaling in the thermalization domain. Even though Kolmogorov's scaling is not present in the other curves with smaller Reynolds numbers, the equipartition scaling law is still observable in the large scales. The smallest Reynolds number was then used to compute the DNSs of the right panel of Fig. 10 where the wave number varies at fixed Reynolds number. The equipartition scaling of the energy spectrum can be observed on the three forcing wave numbers used. The curve with the largest forcing scale, $k_f = 59\sqrt{3}$, shows that the energy spectrum follows a k^2 scaling.

We now turn to the temporal correlation of the flows presented in Fig. 11. The left panel shows the dependence on viscosity of the correlation time for flows forced at $k_f = 11\sqrt{3}$. The correlations are computed using the algorithm presented in Sec. III A 1. In the small scales, the correlation time

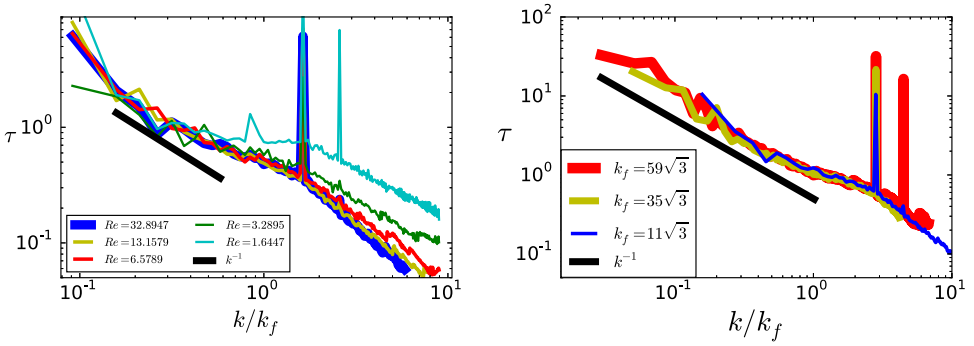

FIG. 11. Correlation time of Taylor-Green symmetric DNS of the forced Navier-Stokes equation. (Left) Different Reynolds numbers at fixed forcing wave number $k_f = 11\sqrt{3}$. (Right) Different forcing wave numbers $k_f \in \{11\sqrt{3}; 35\sqrt{3}; 59\sqrt{3}\}$ at fixed Reynolds number.

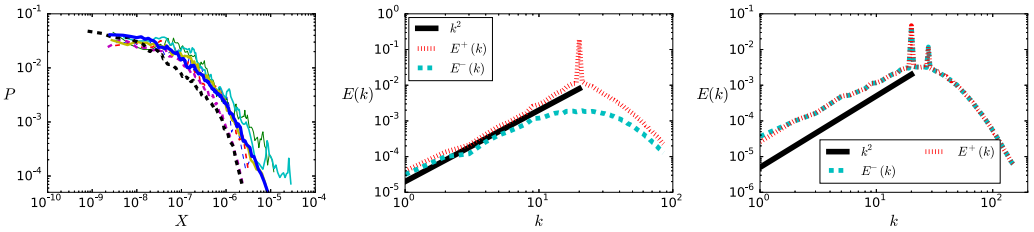

FIG. 12. Statistical characteristics of general-periodic DNSs of the Navier-Stokes equation. (Left) ABC forcing, PDF of modes before the forcing scale. The full lines represent the positive helical components of the velocity, and the dashed lines represent the negative helical components of the velocity. (Center) ABC forcing, energy spectrum of positive and negative helical components of the velocity. (Right) CBA forcing, energy spectrum of positive, and negative helical components of the velocity.

slowly decreases as viscosity decreases, whereas the correlation time rapidly stabilizes on a k^{-1} power law in the large scales. The major peak observed in the flow does not correspond to the forcing wave vector, which is not located on the planes used to compute the correlation time. This peak corresponds to a harmonic of the forcing located in one of the planes used in the correlation time procedure. At high Reynolds number, in the large scales, the correlation time aligns on a curve, which is consistent with the energy-based correlation time k^{-1} scaling.

The k^{-1} scaling law of the correlation time can be observed in the right panel of Fig. 11, which shows the correlation time for three scale separations $k_f = \{11\sqrt{3}; 35\sqrt{3}; 59\sqrt{3}\}$. The Reynolds number used in these DNSs is based on the smallest viscosity used in the left panel of Fig. 11. The correlation times for the three scale separations collapse on the k^{-1} power law. The data at the largest forcing wave number $k_f = 59\sqrt{3}$ shows a trend which strongly agrees with the energy-based correlation time k^{-1} scaling.

B. Helical flows: ABC flows

In order to study the impact of helicity on the velocity modes in large scales, DNSs were carried out on general-periodic flows solutions of the NSE given at Eq. (2) with an ABC forcing [28]

$$\begin{aligned} F_x^{ABC} &= F_0(C \sin k_f z + B \cos k_f y), \\ F_y^{ABC} &= F_0(A \sin k_f x + C \cos k_f z), \\ F_z^{ABC} &= F_0(B \sin k_f y + A \cos k_f y), \end{aligned} \tag{22}$$

where F_0 is the intensity of the forcing. The three dimensionless parameters A, B, and C were set to one. The main characteristic of ABC flows is their Beltrami property: $\nabla \times F^{ABC} = k_f F^{ABC}$. This property makes them exact (but in general unstable) solutions of the TEE. All the ABC DNSs presented are done at $k_f = 20$. A nonhelical variant of the ABC forcing, that we will refer to as the CBA forcing, can be built by switching the sine components of the ABC forcing to cosine components:

$$\begin{aligned} F_x^{CBA} &= F_0(C \cos k_f z + B \cos k_f y), \\ F_y^{CBA} &= F_0(A \cos k_f x + C \cos k_f z), \\ F_z^{CBA} &= F_0(B \cos k_f y + A \cos k_f y). \end{aligned} \tag{23}$$

The CBA forcing has already been used as a nonhelical reference of the ABC flow in Ref. [29]. At fixed coefficients, the CBA forcing has the same energy as the ABC forcing but does not have any helicity whereas the ABC forcing is fully helical.

The PDFs of the positive and negative helical components of the modes in the large scales are presented in the left panel of Fig. 12 for DNSs of the NSE with an ABC forcing. The positive helical component of the velocity is represented with full lines, and the negative helical component

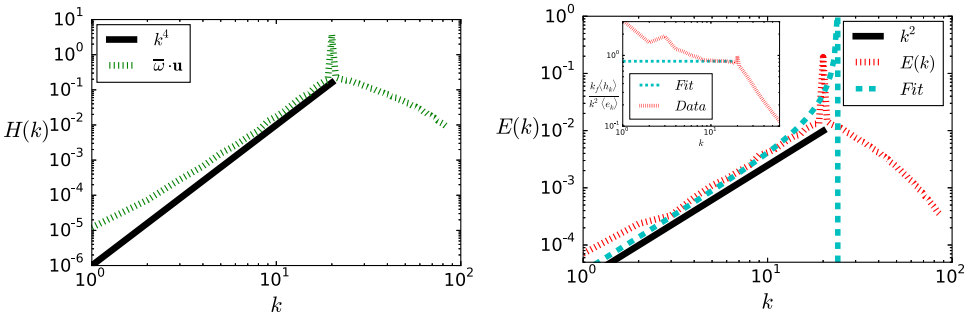

FIG. 13. Spectrum of general-periodic DNSs of the Navier-Stokes equation with an ABC forcing. (Left) Helicity spectrum in the dotted line and the absolute equilibrium power law in the full line. (Right) Energy spectrum in the dotted line with absolute equilibrium power law in the full line and absolute equilibrium fit in the dashed line. The insert represents the local determination of the Kraichnan number, $k_f\langle h_{\boldsymbol{k}}\rangle/(k^2\langle e_{\boldsymbol{k}}\rangle)$, resulting from Eq. (10). The asymptotic value is used to make the absolute equilibrium fit.

of velocity is represented with dashed lines. All PDFs plateau near zero and have a fast decay at high values. Because general-periodic DNSs do not reach the same scale separation and Reynolds number as TG symmetric DNSs, the comparison with the χ^2_2 distribution is not as clear as in Fig. 9. The PDFs of the two helical components do not have the same exponential tail as observed in absolute equilibrium solutions of the TEE. Since solutions of the NSE are not as helical as the solution of the TEE considered in the previous section, the separation of the tail of the distributions is not as wide as in the case of absolute equilibrium solutions of the TEE. The center panel of Fig. 12 represents the energy spectrum of the two helical components of DNSs of the NSE with an ABC forcing. The positive helical component of the velocity has more energy than its negative counterpart, which is consistent with the separation of the tail of the distribution presented in the left panel. Both components follow a k^2 scaling consistent with equipartition. In the large scales, the general features of the modes match the properties of absolute equilibrium solutions of the TEE. The right panel of Fig. 12 represents the energy spectrum of the two helical components of DNSs of the NSE with a CBA forcing. The energy spectrum is not as close to the k^2 scaling as the energy spectrum resulting from an ABC forcing. We note that the energy spectrum of the nonhelical TG symmetric flows, presented in the right panel of Fig. 10, deviates from the k^2 scaling at the smallest scale separations. The convergence study carried out in the right panel of Fig. 4 indicates that such a deviation can happen at small scale separations.

The left panel of Fig. 13 represents the helicity spectrum of a solution of the Navier-Stokes equation with an ABC forcing. In the scales slightly larger than the forcing scale, the helicity spectrum is in good agreement with the k^4 power law of the absolute equilibrium prediction. But in the largest scale, the helicity spectrum has a deviation from the k^4 power law.

To compare absolute equilibrium solutions of the TEE and the large-scale modes of solutions of the NSE, we introduce an analog of the Kraichnan number for the NSE. The equivalent of the maximal wave number k_M in the truncated Euler problem is assumed to be the forcing wave number k_f in the case of the NSE. Two expressions can be used to compute the local Kraichnan number: either $k_f\langle h_{\boldsymbol{k}}\rangle/(k^2\langle e_{\boldsymbol{k}}\rangle)$ coming from Eq. (9) or $k_f(\langle e^+_{\boldsymbol{k}}\rangle - \langle e^-_{\boldsymbol{k}}\rangle)/[k(\langle e^+_{\boldsymbol{k}}\rangle + \langle e^-_{\boldsymbol{k}}\rangle)]$ coming from Eq. (10). Both expressions are equivalent and give the same numeric results presented in the insert of the right panel of Fig. 13. The local Kraichnan number is not independent of the wave number and has an important peak in the large scales. As the wave number reaches the forcing wave number, the local local Kraichnan number goes to a constant value equal to 0.83 . The result is consistent with the $|\mathrm{Kr}| \leqslant 1$ bound of absolute equilibrium solutions. This asymptotic value is then used to plot the absolute equilibrium fit in the right panel of Fig. 13. In the large scales, the data from the DNSs are slightly above the fit, while the data are below the fit near the forcing wave

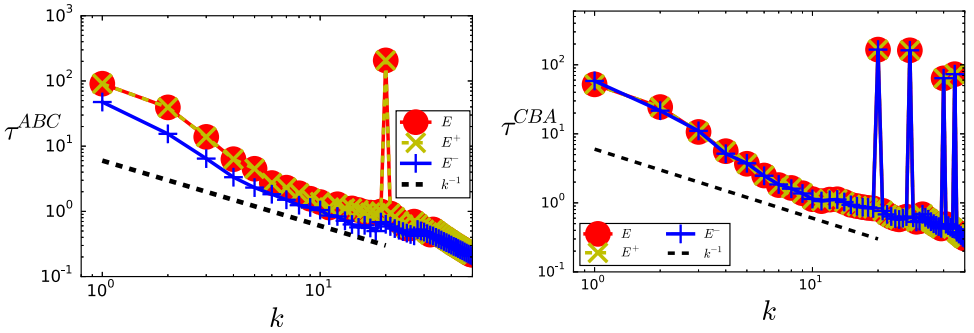

FIG. 14. Correlation time of general-periodic DNSs of the Navier-Stokes equation. (Left) ABC forcing. (Right) CBA forcing.

number. The difference between the fit and the data near the forcing wave number can be related to the presence of the forcing. The difference found in the large scales could be related to finite size effects such as three-mode interaction with the forcing like in Ref. [12].

The correlation time of DNSs of the NSE with an ABC forcing increases in the large scales as shown in the left panel of Fig. 14. In the inertial domain, the correlation time decreases as the wave number increases. These observations are consistent with the results of helical DNSs of the TEE and the TG symmetric DNSs of the the NSE. However, the correlation time has some elements which do not appear in the helical DNSs of the TEE presented in Fig. 8. The correlation time of positive helical components of the velocity is always greater than its negative counterpart, especially in the large scales. This separation between the correlation time of the different helical components is not observed in the right panel of Fig. 14 representing DNSs of the NSE with a CBA. Contrary to the ABC forced flow, the correlation times of CBA forced flows exhibit a set of peaks in the inertial domain corresponding to harmonics of the forcing. For the ABC forcing and CBA forcing, the correlation time in the large scales deviates from the k^{-1} power law observed in DNSs of TEE. However, for similar scale separations, the results from TG DNSs also deviated from the k^{-1} power law in the left panel of Fig. 11. Figure 15 compares the correlation times of the ABC forcing and CBA forcing. The correlation time of the two flows seems very close when observing the energy spectrum presented in the left panel. However, the ratio presented in the right panel shows that the correlation times of the helical ABC forcing are larger than their nonhelical CBA counterparts. The differences between the two correlation times reaches nearly 20% for all the wave numbers smaller than the forcing wave number and is much more important in the two shells with smallest k.

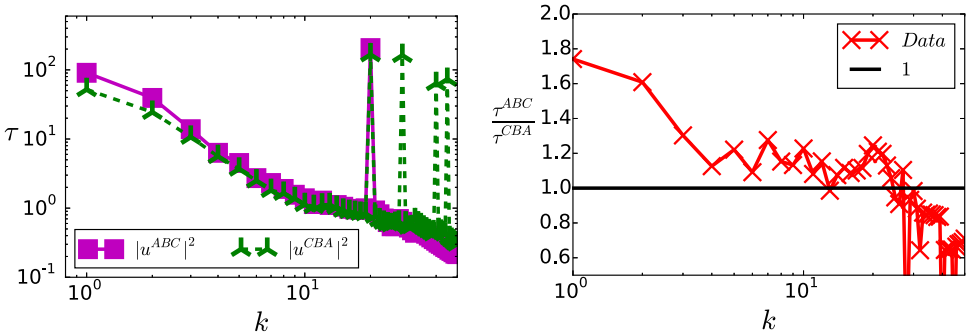

FIG. 15. Comparison of the correlation time of $[0;2\pi]^3$-periodic DNSs solutions of the Navier-Stokes equation forced with ABC and CBA forcings. (Left) Correlation time. (Right) Ratio of the correlation time.

V. CONCLUSION

In this study, we examined analytically and numerically the temporal dynamics of absolute equilibrium solutions of the truncated Euler equation and compared them to the large-scale modes of solutions of the Navier-Stokes equation. We calculated the Eulerian parabolic autocorrelation time of velocity modes of absolute equilibrium solutions of the TEE under the assumption that the velocity modes follow a Boltzmann-Gibbs distribution. For nonhelical or slightly helical flows, $|\mathrm{Kr}| < 0.8$, the correlation time decreases inversely proportionally to the wave number and the square root of energy $\tau \propto 1/(kE^{1/2})$. On the other hand, when the flow is highly helical $|\mathrm{Kr}| > 0.9$, the correlation time depends on the helicity and is inversely proportional to the square root of the wave number $\tau \propto 1/(k^{1/2}H^{1/2})$. This new power law behavior holds for wave numbers that satisfy $(1 - \mathrm{Kr})\ln(1 - \mathrm{Kr}) \ll k/k_M \ll 1$, while the k^{-1} is recovered at even smaller wave numbers. These results and the assumptions on which they were based were tested against the results of DNSs of the TEE showing agreement: the PDFs of the modes of velocity displayed the characteristics of Gaussian variables, their energy spectrum followed the laws predicted by the absolute equilibrium theory, and the two predicted power laws for the correlation time for helical and nonhelical flows were recovered. We have thus demonstrated that, in the long time limit, the TEE thermalizes to an absolute equilibrium state whose statistics and time correlation can be derived from a Boltzmann-Gibbs distribution.

The results are less clear for the scaling law of the correlation in the large scales of the forced NSE. Simulations using the nonhelical TG geometry, which allowed us to reach larger scale separation, displayed considerable agreement with the absolute equilibrium. The velocity modes at large scales followed Gaussian distributions with standard deviations consistent with equipartition; the correlation time followed a power law compatible with the k^{-1} scaling. This is in agreement with the absolute equilibrium at large scales. The agreement, however, was less strong with the results of DNSs of general-periodic flows. The large-scale spectra were compatible with the absolute equilibrium predictions for a limited range. The largest scales deviated significantly, being more energetic and more helical than predicted. Note that this deviation was also observed in Ref. [10]. Furthermore, while the correlation time of the helical flows was shown to decrease with helicity as in thermalization theory, the measured correlation time deviates significantly from the predicted k^{-1} and $k^{-1/2}$ power laws. We note, however, that a similar deviation is also observed in nonhelical TG symmetric DNSs at the smallest boxes used (see Fig. 10), so these deviations could be due to insufficient scale separation.

The reason for which the largest scales of Navier-Stokes solutions deviate from absolute equilibrium still remains an open question. As discussed above, a possible cause for this deviation could be related to the range in the large scales or the range of the Reynolds number. For the moment, however, we cannot exclude the possibility that large scales lack universality with respect to forcing or that large scales instabilities spoil the absolute equilibrium properties. Our results could also be tested in laboratory experiment for turbulent flows forced at small scale as has already been done for capillary wave turbulence in Ref. [30].

ACKNOWLEDGMENTS

This work was granted access to the HPC resources of MesoPSL financed by the Region Ile de France and the project Equip@Meso (reference ANR-10-EQPX-29-01) of the programme Investissements d'Avenir supervised by the Agence Nationale pour la Recherche and the HPC resources of GENCI-TGCC-CURIE and GENCI-CINES-JADE (Project No. x20162a7620) where the present numerical simulations have been performed. The authors are grateful to Pablo Mininni and Patricio Clark di Leoni for their useful discussions on spatio-temporal spectra.

APPENDIX A: CORRELATION TIME—PARABOLIC HYPOTHESIS

The derivation of the correlation time can be done using a projection operator on incompressible flows, as in Ref. [8]. However, this method is not able to assess the properties of the helical

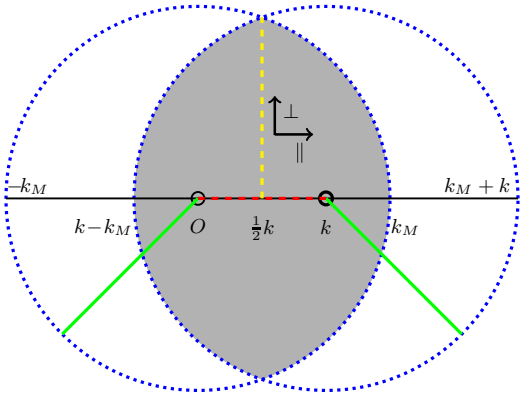

FIG. 16. Diagram of a cut of the integration domain. The dark surface corresponds to the integration domain. The dotted lines correspond to the limit of the circles of radius k_M and of center 0 or k. The thick full line corresponds to radii of the previously described circles. The dark dashed line corresponds to the distance between the center of the two circles. The bright dashed line corresponds to the maximal length possible for $q_\perp$.

components of the velocity. In order to quantify these properties, the standard framework is the Craya-Herring-Lesieur helical basis [16–18]. Within this decomposition, the TEE is expressed as

$$\left(\partial_t u_{\boldsymbol{k}}^{s_k}\right)^* = \sum_{\substack{\boldsymbol{k}+\boldsymbol{p}+\boldsymbol{q}=0 \\ s_p,\, s_q}} (s_p p - s_q q)\left(-\frac{1}{4}\boldsymbol{h}_{\boldsymbol{k}}^{s_k} \cdot \boldsymbol{h}_{\boldsymbol{p}}^{s_p} \times \boldsymbol{h}_{\boldsymbol{q}}^{s_q}\right) u_{\boldsymbol{p}}^{s_p} u_{\boldsymbol{q}}^{s_q} = \sum_{\substack{\boldsymbol{k}+\boldsymbol{p}+\boldsymbol{q}=0 \\ s_p,\, s_q}} C_{\boldsymbol{kpq}}^{s_k s_p s_q} u_{\boldsymbol{p}}^{s_p} u_{\boldsymbol{q}}^{s_q}, \tag{A1}$$

where $s_{\boldsymbol{k}}$ denotes the sign of the helical component at mode $\boldsymbol{k}$, $u_{\boldsymbol{k}}^{s_k}$ denotes the helical component of the velocity of sign $s_{\boldsymbol{k}}$ at mode $\boldsymbol{k}$, and $\boldsymbol{h}_{\boldsymbol{k}}^{s_k}$ denotes the complex unitary helical vector of the Craya-Herring-Lesieur basis satisfying $\boldsymbol{\nabla} \times \boldsymbol{h}_{\boldsymbol{k}}^{s_k} = s_{\boldsymbol{k}} k \boldsymbol{h}_{\boldsymbol{k}}^{s_k}$. The Craya-Herring-Lesieur tensor $C_{\boldsymbol{kpq}}^{s_k s_p s_q}$ is symmetric on its last two variables, $C_{\boldsymbol{kpq}}^{s_k s_p s_q} = C_{\boldsymbol{kqp}}^{s_k s_q s_p}$, and also satisfies $C_{\boldsymbol{kpp}}^{s_k s_p s_p} = 0$. With the Craya-Herring-Lesieur helical decomposition, the average correlation of the temporal derivative of the velocity can be derived with the assumption that all helical components are independent Gaussian variables. The derivation leads to

$$\left\langle \left| \partial_t \bar{u}_{\boldsymbol{k}}^{s_k} \right|^2 \right\rangle = \left\langle \sum_{\substack{\boldsymbol{k}+\boldsymbol{p}_1+\boldsymbol{q}_1=0 \\ s_{p_1},\, s_{q_1}}} \sum_{\substack{\boldsymbol{k}+\boldsymbol{p}_2+\boldsymbol{q}_2=0 \\ s_{p_2},\, s_{q_2}}} C_{\boldsymbol{kp_1q_1}}^{s_k s_{p_1} s_{q_1}} u_{\boldsymbol{p}_1}^{s_{p_1}} u_{\boldsymbol{q}_1}^{s_{q_1}} \left[C_{\boldsymbol{kp_2q_2}}^{s_k s_{p_2} s_{q_2}} u_{\boldsymbol{q}_2}^{s_{p_2}} u_{\boldsymbol{q}_2}^{s_{p_2}} \right]^* \right\rangle \tag{A2}$$

$$= \sum_{s_1,\, s_2} \mathcal{S}^{s_1 s_2} \quad \text{where} \quad \mathcal{S}^{s_1 s_2} = \sum_{\substack{\boldsymbol{k}+\boldsymbol{p}+\boldsymbol{q}=0 \\ s_p = s_1,\, s_q = s_2}} 2 \left| C_{\boldsymbol{kpq}}^{s_k s_p s_q} \right|^2 \left\langle \left| \boldsymbol{u}_{\boldsymbol{p}}^{s_p} \right|^2 \right\rangle \left\langle \left| \boldsymbol{u}_{\boldsymbol{q}}^{s_q} \right|^2 \right\rangle, \tag{A3}$$

where $\mathcal{S}^{s_1 s_2}$ corresponds to the sum of the triadic interact of sign s_1 and s_2.

In Eq. (A3), the truncation condition, $\boldsymbol{u}(k > k_M) = 0$, has not been applied to the velocity fields. The velocity appears in the equation within the expression of the average energy with two indices $\boldsymbol{p}$ and $\boldsymbol{q}$, and therefore the summation must be done at $p \leqslant k_M$ and $q \leqslant k_M$. The domain prescribed by these conditions corresponds to the intersection of two spheres of radii k_M and centers $\boldsymbol{p}$ and $\boldsymbol{q}$. The triadic condition, $\boldsymbol{k} + \boldsymbol{p} + \boldsymbol{q} = 0$, also implies that the summation over $\boldsymbol{p}$ and $\boldsymbol{q}$ can be done over $\boldsymbol{q}$ at fixed $\boldsymbol{p} = \boldsymbol{k} - \boldsymbol{q}$. The domain of summation is represented in Fig. 16. This domain is invariant by rotation along the axis defined by $\boldsymbol{k}$ in Fig. 16. The centers of the two spheres are also located on this direction. The coefficients of the sum in Eq. (A3) are unaffected by the rotation. The summation can thus be performed with the variables $q_\perp$ and $q_\parallel$ where $q_\perp$ is the projection of the wave vector

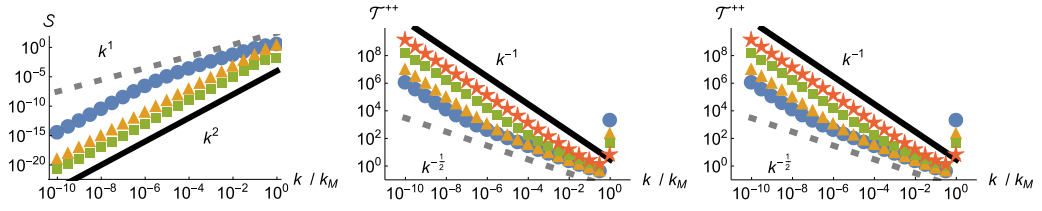

FIG. 17. Triadic interaction as a function of the wave number and associated correlation time. (Left) At $\mathrm{Kr} = 1\text{–}10^{-6}$, $\mathcal{S}^{--}$ plotted with squares, $\mathcal{S}^{+-}$ plotted with triangle, $\mathcal{S}^{++}$ plotted with disks, k^1 plotted with a dashed line, k^2 plotted with a full line. (Center) $\mathcal{S}^{++}$ plotted at $\mathrm{Kr} = 1\text{–}10^{-8}$ with disks, at $\mathrm{Kr} = 1\text{–}10^{-6}$ with triangles, at $\mathrm{Kr} = 1\text{–}10^{-2}$ with squares, at $\mathrm{Kr} = 1\text{–}10^{-2}$ with stars, k^1 with a dashed line, k^2 with a full line. (Right) $\mathcal{T}^{++}$ plotted at $\mathrm{Kr} = 1\text{–}10^{-8}$ with disks, at $\mathrm{Kr} = 1\text{–}10^{-6}$ with triangles, at $\mathrm{Kr} = 1\text{–}10^{-2}$ with squares, at $\mathrm{Kr} = 1\text{–}10^{-2}$ with stars, $k^{-\frac{1}{2}}$ with a dashed line, k^{-1} with a full line.

along the plane orthogonal to $\boldsymbol{k}$ and $q_\parallel$ is the projection of the wave vector along the axis of rotation. Taking this new coordinate system, the derivation can be simplified by converting the discrete sum into an integral using the equivalence

$$\sum_{\boldsymbol{k}+\boldsymbol{p}+\boldsymbol{q}=0} \Longleftrightarrow \int_{-(1-\frac{1}{2}m)}^{1-\frac{1}{2}m} dq_\parallel \int_0^{1-\left(|q_\parallel|+\frac{1}{2}m\right)^2} \pi\, dq_\perp^2 \quad \text{where} \quad m = \frac{k}{k_M}. \tag{A4}$$

This integral can be computed exactly when $\mathrm{Kr} = 0$ for $m \ll 1$, the parabolic correlation time is then expressed as

$$\tau_{\boldsymbol{k}}^{s_k} = \sqrt{\frac{\left\langle \left| u_{\boldsymbol{q}}^{s_q} \right|^2 \right\rangle}{\left\langle \left| \partial_t \bar{u}_{\boldsymbol{k}}^{s_k} \right|^2 \right\rangle}} = \sqrt{\frac{45\alpha}{112}} \frac{1}{k} = \sqrt{\frac{15\pi C_N}{14}} \frac{1}{k\sqrt{E_{\mathrm{tot}}}}. \tag{A5}$$

Since $E_{\mathrm{tot}} \propto \alpha^{-1}$, the correlation time follows the energy-based scaling law.

When $\mathrm{Kr} \neq 0$, the final integral can be computed using Mathematica for the different helical triadic interactions as shown in Fig. 17 for highly helical flows. Instead of computing all the terms corresponding to all different possible triads in the sum, the graph shows the computation triad with different helical signs. The left plot of Fig. 17 shows three possible sums: $\mathcal{S}^{++}$ plotted with disks, $\mathcal{S}^{+-}$ plotted with triangles, and $\mathcal{S}^{--}$ plotted with squares. The $\mathcal{S}^{-+}$ sum has exactly the same values as the $\mathcal{S}^{+-}$ sum for symmetry reasons. The $\mathcal{S}^{++}$ sum dominates the other terms and has a k^1 scaling at large wave numbers consistent with a helicity-based correlation time, and a k^2 scaling at small wave numbers consistent with an energy-based correlation time. All other terms follow a k^2 scaling. The center plot of Fig. 17 shows the evolution of the $\mathcal{S}^{++}$ for different Kraichnan numbers. As the Kraichnan number goes to one, the domain where the sum follows a k^2 scaling widens. The right plot of Fig. 17 shows the evolution of the correlation time, $\mathcal{T}^{++}$, built using the sum $\mathcal{S}^{++}$. Its evolution is consistent with the evolution of the correlation time of the full velocity field presented in the left panel of Fig. 1.

When the Kraichnan number goes to one, the *plus-plus* triadic interaction dominates the nonlinear interaction in the TEE. Whether $m \ll \epsilon \ll 1$ or $\epsilon \ll m \ll 1$, the correlation time follows the asymptotic expression

$$\mathcal{S}^{++} = 2\pi k^2 \alpha^{-2} \frac{-2\ln\epsilon}{m - A\epsilon\ln\epsilon} \quad \text{with} \quad A = \frac{15}{8} \quad \text{thus}$$

$$\mathcal{T}^{++}(\boldsymbol{k}, s_{\boldsymbol{k}}) = \sqrt{\frac{\left\langle \left| \boldsymbol{u}_{\boldsymbol{k}}^{s_k} \right|^2 \right\rangle}{\mathcal{S}^{++}}} = \sqrt{\frac{A(1-\mathrm{Kr}) - \frac{k}{k_M \ln(1-\mathrm{Kr})}}{4\pi\alpha^{-1}k^2\left(1 - s_{\boldsymbol{k}}\mathrm{Kr}\frac{k}{k_M}\right)}}. \tag{A6}$$

In the domain where $(1 - \mathrm{Kr}) \ll \frac{k}{k_M} \ll 1$, the correlation time follows a helicity-based scaling law.

APPENDIX B: TAYLOR-GREEN SYMMETRIES

In addition to the conditions listed below Eq. (19), TG symmetries [23] impose that

$$u^y(k_x,k_y,k_z) = (-1)^{p+1}u_x(k_y,k_x,k_z) \quad \text{and} \quad u_z(k_x,k_y,k_z) = (-1)^{p+1}u_z(k_y,k_x,k_z), \tag{B1}$$

where p characterizes the parity of the mode: $p = 1$ if k_x, k_y, k_z are all even and $p = 0$ if k_x, k_y, k_z are all odd.

Since the flows studied are also incompressible, they also satisfy $\boldsymbol{\nabla}\cdot\boldsymbol{u} = 0 \iff k_x u_x + k_y u_y + k_z u_z = 0$.

In a few special cases, modes of TG symmetric flows depend on only one independent variable:

1. $k_x = k_y$ and $r = 0$: $\boldsymbol{u}^{\text{odd}}(k_x,k_x,k_z) = (\boldsymbol{e}_x - \boldsymbol{e}_y)\psi_0(k_x,k_z)$ where ψ_0 is a real field.
2. $k_x = k_y$ and $r = 1$: $\boldsymbol{u}^{\text{even}}(k_x,k_x,k_z) = (k_z(\boldsymbol{e}_x + \boldsymbol{e}_y) - (k_x + k_y)\boldsymbol{e}_z)\psi_1(k_x,k_x,k_z)$ where ψ_1 is a real field.
3. $k_x = 0$: $\boldsymbol{u}(0,k_y,k_z) = (k_z\boldsymbol{e}_y - k_y\boldsymbol{e}_z)\psi_2(k_y,k_z)$ where ψ_2 is a real field.
4. $k_y = 0$: $\boldsymbol{u}(k_x,0,k_z) = (k_z\boldsymbol{e}_x - k_y\boldsymbol{e}_z)\psi_3(k_x,k_z)$ where ψ_3 is a real field.
5. $k_z = 0$: $\boldsymbol{u}(k_x,k_y,0) = (k_y\boldsymbol{e}_x - k_x\boldsymbol{e}_y)\psi_4(k_x,k_y)$, where ψ_4 is a real field satisfying $\psi_4(k_y,k_x) = -\psi_4(k_x,k_y)$.

The vectors $\boldsymbol{e}_\alpha$ with $\alpha \in \{x;y;z\}$ denote the directions of the Cartesian basis.

In the other cases, the TG symmetric modes of flows only depend on two independent variables—$\phi(k_x,k_y,k_z)$ and $\phi(k_y,k_x,k_z)$, where ϕ is a real field—and can be written as

$$\boldsymbol{u}(k_x,k_y,k_z) = (k_z\boldsymbol{e}_x - k_x\boldsymbol{e}_z)\phi(k_x,k_y,k_z) + (-1)^{p+1}(k_z\boldsymbol{e}_y - k_y\boldsymbol{e}_z)\phi(k_y,k_x,k_z). \tag{B2}$$

APPENDIX C: CHI-SQUARED DISTRIBUTION

A Gaussian distribution of average μ and standard derivation σ has a probability density function defined by

$$G(X|\mu,\sigma) = \frac{1}{\sqrt{2\sigma^2\pi}}\, e^{-\frac{(X-\mu)^2}{2\sigma^2}}. \tag{C1}$$

Chi-squared distributions are defined using g independent Gaussian variables. Let $(G_i)_{i\in[\![1;g]\!]}$ be independent, centered ($\mu = 0$), reduced ($\sigma = 1$) Gaussian variables. The sum of their squares, $X = \sum_{i=1}^{g} G_i^2$, is distributed according to the chi-squared distribution with g degrees of freedom denoted as χ_g^2 and defined by

$$\chi_g^2(X) = \frac{1}{2^{\frac{g}{2}}\Gamma_{\text{Euler}}\left(\frac{g}{2}\right)} X^{\frac{g}{2}-1}e^{-\frac{X}{2}}, \tag{C2}$$

where Γ_{Euler} denotes Euler's Gamma function. The power law of the probability density function at small X gives the number of degrees of freedom of the system, and the exponential fit at large X validates the Gaussian decay of the probability density function.

$$\log\chi_g^2(X) \underset{X\to 0}{=} \left(\frac{g}{2} - 1\right)\log(X) \quad \text{thus} \quad g \underset{X\to 0}{=} 2\left[\frac{\log\chi_g^2(X)}{\log(X)} + 1\right]. \tag{C3}$$

APPENDIX D: COMPUTATION OF THE CORRELATION TIME

In order to produce spatio-temporal spectrum, the velocity field is outputted at a regular time interval. These outputs form a data set of the velocity field in the $\boldsymbol{k}$-t space. However, keeping in memory the entire N^3 DNSs, N being the resolution, is too demanding in storage memory. To reduce the volume of the data set without losing the properties of the different modes, only the six planes $k_x = \{0;1\}$, $k_y = \{0;1\}$, and $k_z = \{0;1\}$ are outputted for the TG symmetric TYGRE code, and only the three planes $k_x = 0$, $k_y = 0$, and $k_z = 0$ are outputted for the general-periodic GHOST code. The velocity time series are then multiplied by an apodization function [31] and Fourier-transformed

to form a data set in the $\boldsymbol{k}$-ω space. The power spectrum $s(\boldsymbol{k},\omega)$ is then computed by taking the modulus square of the velocity and summing over the different Cartesian directions. The isotropic power spectrum $S(k,\omega)$ is computed by summing the power spectrum over the modes of same wave number. A binning of spacing of one is used to compute the isotropic power spectrum. The closest integer smaller than $k+\frac{1}{2}$ is used to define the bin number. The left panel of Fig. 4 represents the power spectrum of a truncated Euler DNSs computed using this method. The correlation function $\Gamma(k,t)$ is then computed using Wiener-Khinchin theorem by performing a Fourier transform of the isotropic power spectrum and normalizing the function. The right panel of Fig. 4 represents the correlation function of a truncated Euler DNSs computed using this method.

Finally, the correlation time can be computed by doing a fit of the correlation function in a well-resolved domain as shown in the left panel of Fig. 5. The time where the correlation function reaches half-height, $\tau_{\frac{1}{2}}$, can be evaluated numerically. The same algorithm can be used to find the correlation function of the positive and negative helical modes of the velocity field using Eq. (10). The steps of the procedure are summed up in the algorithm presented below. Here $D\mathcal{F}$ denotes the discrete Fourier transform, $D\mathcal{F}^{-1}$ denotes the discrete inverse Fourier transform, $\mathbb{1}$ denotes the characteristic function satisfying $\mathbb{1}(bool)=1$ if $(k-\frac{1}{2}<|\boldsymbol{k}|\leqslant k+\frac{1}{2})$ and 0 otherwise, $apo(n,\Delta t)$ denotes an apodization function, and $Solve[t,\Gamma(k,t),1/2]$ denotes a function that finds the smallest positive t satisfying $\Gamma(k,t)=1/2$.

Require $\boldsymbol{u}(\boldsymbol{k},n\Delta t)$, n, Δt,

(1) $\boldsymbol{u}(\boldsymbol{k},\omega)=D\mathcal{F}[apo(n,\Delta t)\boldsymbol{u}(\boldsymbol{k},n\Delta t)](\omega)$

(2) $s(\boldsymbol{k},\omega)=\sum_i|\boldsymbol{u}_i(\boldsymbol{k},\omega)|^2$

(3) $S(k,\omega)=\sum_{\boldsymbol{k}}\mathbb{1}_k s(\boldsymbol{k},\omega)$

(4) $\gamma(k,t)=D\mathcal{F}^{-1}[S(k,\omega)](t)$

(5) $\Gamma(k,t)=\gamma(k,t)/\gamma(k,0)$

(6) $\tau(k)=Solve[t,\Gamma(k,t),1/2]$

[1] F. H. Champagne, The fine-scale structure of the turbulent velocity field, J. Fluid Mech. **86**, 67 (1978).

[2] Y. Kaneda, T. Ishihara, M. Yokokawa, K. Itakura, and A. Uno, Energy dissipation rate and energy spectrum in high resolution direct numerical simulations of turbulence in a periodic box, Phys. Fluids **15**, L21 (2003).

[3] U. Frisch, *Turbulence: The Legacy of AN Kolmogorov* (AIP, New York, 1996).

[4] A. N. Kolmogorov, The local structure of turbulence in incompressible viscous fluid for very large Reynolds numbers, Math. Phys. Sci. **434**, 9 (1991).

[5] D. Forster, D. R. Nelson, and M. J. Stephen, Large-distance and long-time properties of a randomly stirred fluid, Phys. Rev. A **16**, 732 (1977).

[6] R. H. Kraichnan and S. Chen, Is there a statistical mechanics of turbulence? Physica D: Nonlinear Phenomena **37**, 160 (1989).

[7] R. H. Kraichnan, Helical turbulence and absolute equilibrium, J. Fluid Mech. **59**, 745 (1973).

[8] C. Cichowlas, P. Bonaïti, F. Debbasch, and M. Brachet, Effective Dissipation and Turbulence in Spectrally Truncated Euler Flows, Phys. Rev. Lett. **95**, 264502 (2005).

[9] G. Krstulovic, P. D. Mininni, M. E. Brachet, and A. Pouquet, Cascades, thermalization, and eddy viscosity in helical Galerkin truncated Euler flows, Phys. Rev. E **79**, 056304 (2009).

[10] V. Dallas, S. Fauve, and A. Alexakis, Statistical Equilibria of Large Scales in Dissipative Hydrodynamic Turbulence, Phys. Rev. Lett. **115**, 204501 (2015).

[11] U. Frisch, Zh. S. She, and P. L. Sulem, Large-scale flow driven by the anisotropic kinetic alpha effect, Physica D: Nonlinear Phenomena **28**, 382 (1987).
[12] A. Cameron, A. Alexakis, and M.-E. Brachet, Large-scale instabilities of helical flows, Phys. Rev. Fluids **1**, 063601 (2016).
[13] P. Clark di Leoni, P. J. Cobelli, and P. D. Mininni, The spatio-temporal spectrum of turbulent flows, Eur. Phys. J. E **38**, 136 (2015).
[14] T. D. Lee, On some statistical properties of hydrodynamical and magneto-hydrodynamical fields, Q. Appl. Math. **10**, 69 (1952).
[15] L. D. Landau and E. M. Lifshitz, *Statistical Physics* (Butterworth-Heinemann, Burlington, 1980).
[16] A. Craya, Contribution a l'analyse de la turbulence associée à des vitesses moyennes, Thesis, Université de Grenoble (1957).
[17] J. R. Herring, Approach of axisymmetric turbulence to isotropy, Phys. Fluids **17**, 859 (1974).
[18] M. Lesieur, *Turbulence in Fluids* (Springer Science, New York, 2012).
[19] M. E. Brachet, D. I. Meiron, S. A. Orszag, B. G. Nickel, R. H. Morf, and U. Frisch, Small-scale structure of the Taylor-Green vortex, J. Fluid Mech. **130**, 411 (1983).
[20] A. Pouquet, E. Lee, M. E. Brachet, P. D. Mininni, and D. Rosenberg, The dynamics of unforced turbulence at high Reynolds number for Taylor-Green vortices generalized to MHD, Geophys. Astrophys. Fluid Dyn. **104**, 115 (2010).
[21] P. D. Mininni, A. Alexakis, and A. Pouquet, Nonlocal interactions in hydrodynamic turbulence at high Reynolds numbers: The slow emergence of scaling laws, Phys. Rev. E **77**, 036306 (2008).
[22] P. D. Mininni, D. Rosenberg, R. Reddy, and A. Pouquet, A hybrid MPI-OpenMP scheme for scalable parallel pseudospectral computations for fluid turbulence, Parallel Comput. **37**, 316 (2011).
[23] C. Nore, M. Abid, and M. E. Brachet, Decaying Kolmogorov turbulence in a model of superflow, Phys. Fluids **9**, 2644 (1997).
[24] E. W. Weisstein, *Chi-Squared Distribution* (MathWorld—A Wolfram Web Resource, 2017), http://mathworld.wolfram.com/Chi-SquaredDistribution.html.
[25] P. J. Cobelli, A. Maurel, V. Pagneux, and P. Petitjeans, Global measurement of water waves by Fourier transform profilometry, Exp. Fluids **46**, 1037 (2009).
[26] B. Miquel, A. Alexakis, and N. Mordant, Role of dissipation in flexural wave turbulence: From experimental spectrum to Kolmogorov-Zakharov spectrum, Phys. Rev. E **89**, 062925 (2014).
[27] E. W. Weisstein, *Wiener-Khinchin Theorem* (MathWorld—A Wolfram Web Resource, 2017), http://mathworld.wolfram.com/Wiener-KhinchinTheorem.html.
[28] T. Dombre, U. Frisch, J. M. Greene, M. Henon, A. Mehr, and A. M. Soward, Chaotic streamlines in the ABC flows, J. Fluid Mech. **167**, 353 (1986).
[29] A. Cameron and A. Alexakis, Fate of Alpha Dynamos at Large Rm, Phys. Rev. Lett. **117**, 205101 (2016).
[30] G. Michel, F. Petrelis, and S. Fauve, Observation of Thermal Equilibrium in Capillary Wave Turbulence, Phys. Rev. Lett. **118**, 144502 (2017).
[31] E. W. Weisstein, *Apodization Function* (MathWorld—A Wolfram Web Resource, 2017), http://mathworld.wolfram.com/ApodizationFunction.html.